PHYSICAL REVIEW B **92**, 165104 (2015)

Topological superconducting states in monolayer FeSe/$SrTiO_3$

Ningning Hao and Shun-Qing Shen
Department of Physics, The University of Hong Kong, Pokfulam Road, Hong Kong, China
(Received 2 May 2015; published 5 October 2015)

The monolayer FeSe with a thickness of one unit cell grown on a single-crystal $SrTiO_3$ substrate (FeSe/STO) exhibits striking high-temperature superconductivity with transition temperature T_c over 65 K reported by recent experimental measurements. In this work, through analyzing the distinctive electronic structure, and providing systematic classification of the pairing symmetry, we find that both s- and p-wave pairing with odd parity give rise to topological superconducting states in monolayer FeSe, and the exotic properties of s-wave topological superconducting states have close relations with the unique nonsymmorphic lattice structure which induces the orbital-momentum locking. Our results indicate that the monolayer FeSe could be in the topological nontrivial s-wave superconducting states if the relevant effective pairing interactions are dominant in comparison with other candidates.

DOI: 10.1103/PhysRevB.92.165104 PACS number(s): 74.78.−w, 74.20.Rp, 74.62.Dh, 74.70.Xa

I. INTRODUCTION

Topological superconductors [1–4] and iron-based superconductors [5] have been research focuses of condensed matter physics in recent years. Topological superconductors have a full pairing gap in the bulk and gapless surface or edge Andreev bound states known as Majorana fermions. Recent scanning tunneling microscopy/spectroscopy (STM/S) measurements observed a robust zero-energy bound state at randomly distributed interstitial excess Fe sites in superconducting Fe(Te,Se), and the behavior of zero-energy bound state resembles the Majorana fermion [6]. Theoretically, one possible scenario accounting for this puzzle is that Fe(Te,Se) could be in a topological superconducting (SC) state. If it is the case, we can expect that nontrivial topology can integrate into the SC states in iron-based superconductors.

Recently, some studies [7,8] have revealed that the band structures can be tuned to have nontrivial topological properties in monolayer Fe(Te,Se) and monolayer FeSe/STO. Furthermore, in electron-doped monolayer FeSe/STO, the experimental measurements have observed high temperature superconductivity with T_c over 65 K [9–16]. In analogy to the doped topological insulators, which are strongly believed to be topological superconductors [4,17–19], a natural question arises, can the electron-doped monolayer FeSe/STO be topological superconductors?

In this paper we propose that the electron-doped monolayer FeSe/STO could be an odd-parity topological superconductor in the spin-triplet orbital-singlet s-wave pairing channel [20]. To show this exotic state, we first analyze the distinctive electronic structure of monolayer FeSe/STO, and present a systematic classification of the pairing symmetry in monolayer FeSe/STO from the lattice symmetric group. Second, we discuss the topological properties of such odd-parity SC states, and extract the minimum effective models to capture the essential physics. Third, we calculate the phase diagram of SC states according to different scenarios of effective pairing interaction. Finally, we discuss the experimental signatures of the topological SC states.

II. PAIRING SYMMETRY CLASSIFICATIONS

The lattice structure of monolayer FeSe is shown in Fig. 1(a). The two-Fe unit cell includes two Se and two Fe labeled by A and B. The space group $P4/nmm$ governs the Se-Fe-Se trilayer structure, and belongs to a nonsymmorphic group [21–24]. Indeed, there exists a n-glide plane described by the operator $\{m_z|\frac{1}{2}\frac{1}{2}\}$, which involves a fractional translation $(\frac{1}{2}\frac{1}{2})$ combining with the ab-plane mirror. Centered on an Fe atom [see Fig. 1(a)], eight point group operations E, $2S_4$, $c_2(z)$, $c_2(x)$, $c_2(y)$, and $2\sigma_d$ form a D_{2d} point group. Together with an inversion followed by fractional translations $(\frac{1}{2}\frac{1}{2})$, i.e., $\{i|\frac{1}{2}\frac{1}{2}\}$, they generate all the elements of $P4/nmm$. The 16 operations do not form a point group. However, if the fractional translation $(\frac{1}{2}\frac{1}{2})$ is stripped off, the 16 operations form a point group, which indeed is D_{4h}. It is convenient to classify the pairing symmetry with the irreducible representation (IR) of D_{4h}. For this purpose, one simple way is to recompose the Bloch wave functions in the one-Fe Brillouin zone (BZ).

The glide plane symmetry $\{m_z|\frac{1}{2}\frac{1}{2}\}$ divides the five d orbitals into two groups, (d_{xz},d_{yz}) and $(d_{xy},d_{x^2-y^2},d_{z^2})$, and each group is recomposed to be the eigenstates of the glide plane operation with the definite orbital parities. The tight-binding Hamiltonian can also be decomposed into two parts with inverse orbital parities, which allow us to transfer the two-Fe unit cell picture into a one-Fe unit cell picture [21–23]. In momentum space, the tight-binding Hamiltonian in a one-Fe unit cell picture can be written as

$$H_0=\sum_{\mathbf{k},\sigma}\psi_\sigma^{o\dagger}(\mathbf{k})A_o(k)\psi_\sigma^o(\mathbf{k})+\sum_{\mathbf{k},\sigma}\psi_\sigma^{e\dagger}(\mathbf{k})A_e(k)\psi_\sigma^e(\mathbf{k}). \quad (1)$$

Here the first/second term has odd/even orbital parity under the glide plane operation. $\psi_\sigma^o(k)=[d_{xz,\sigma}(\mathbf{k}),d_{yz,\sigma}(\mathbf{k}),d_{x^2-y^2,\sigma}(\mathbf{k}),d_{xy,\sigma}(\mathbf{k}),\ d_{z^2,\sigma}(\mathbf{k})]^T$ with $d_{m,\sigma}(\mathbf{k})$ denoting the electron annihilation operator at the mth orbital with momentum $\mathbf{k}$ and spin σ. $\psi_\sigma^e(\mathbf{k})=\psi_\sigma^o(\mathbf{k}+\mathbf{Q})$ and $A_e(\mathbf{k})=A_o(\mathbf{k}+\mathbf{Q})$ with $\mathbf{Q}=(\pi,\pi)$ (see Appendix A for details). The energy spectra from Eq. (1) are shown in Fig. 1, in which Fig. 1(e) is consistent with observations of the angle-resolved photoemission

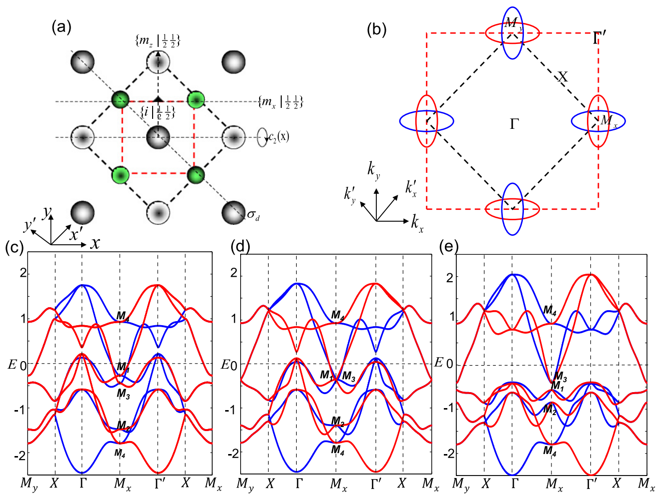

FIG. 1. (Color online) (a) The Se-Fe-Se trilayer structure. The black/green balls with deep and light filling label Fe/Se atoms. Here the deep/light filling Se atoms are above/below the Fe plane. The red/black dashed squares label the one-Fe/two-Fe unit cells. (b) The Fermi surface of monolayer FeSe/STO is schematically illustrated. The red/blue electron pockets have odd/even orbital parity. The red/black dashed squares label the one-Fe/two-Fe Brillouin zone. The evolution of the band structure from (c) the free-standing monolayer FeSe to (d) monolayer FeSe/STO with small tensile strain, and to (e) monolayer FeSe/STO with large tensile strain. The red/blue color labels the spectrum with odd/even orbital parity.

spectroscopy (ARPES) [10,11], and the chemical potential is set to satisfy that 10% electrons is doped per Fe clarified by experiments [10–12]. The fundamental difference between Figs. 1(c) and 1(f) is referred to the band-renormalization effect induced by the strain from the STO substrate, which strongly modulates the hopping parameters between the (d_{xz},d_{yz},d_{xy}) orbitals and switches the positions of two doubly degenerate points M_1 and M_3 at the M_x high symmetric point, where the M_1 point mainly has (d_{xz},d_{yz}) orbital weight and the M_3 point mainly has d_{xy} orbital weight. This picture is the most natural and simplest to account for the distinctive electronic structure of monolayer FeSe/STO compared to other scenarios [25–27].

The SC order parameters should follow the IRs of the symmetry group of the system. It is safe to use D_{4h} to do so in the picture of one-Fe unit cell according to our aforementioned arguments. There exist two kinds of symmetry-allowed Cooper pairs, i.e., $(\mathbf{k},-\mathbf{k})$ and $(\mathbf{k},-\mathbf{k}+\mathbf{Q})$ pairing channels. Previously, the $(\mathbf{k},-\mathbf{k}+\mathbf{Q})$ pairing channels are proposed to coexist with $(\mathbf{k},-\mathbf{k})$ pairing channels to explain the nodeless and sign-change gap structures in iron-based superconductors [21,22]. The price for coexistence of both kinds of pairings is that the orbital parities are mixed and the spatial inversion symmetry is broken. Here we focus on an SC state with only one IR in the $(\mathbf{k},-\mathbf{k})$ pairing channel and leave to discuss the irrelevant $(\mathbf{k},-\mathbf{k}+\mathbf{Q})$ pairing channel in Appendix B. Moreover, we only need to consider the pairings between the three t_{2g} orbitals as the orbital weight for E_g orbitals are neglectable on the Fermi surfaces [28]. Define the Nambu basis, $\Psi(\mathbf{k})=[\{d_\uparrow(\mathbf{k})\},\{d_\downarrow(\mathbf{k})\},\{d_\downarrow^\dagger(-\mathbf{k})\},\{-d_\uparrow^\dagger(-\mathbf{k})\}]^T$ with $\{d_\sigma(\mathbf{k})\}=\{d_{xz,\sigma}(\mathbf{k}),d_{yz,\sigma}(\mathbf{k}),d_{xy,\sigma}(\mathbf{k})\}$. The pairing term in the Bogoliubov–de Gennes (BdG) Hamiltonian can be expressed as

$$H_p=\sum_{\mathbf{k}}\Psi^\dagger(\mathbf{k})\Delta(\mathbf{k})\tau_x\Psi(\mathbf{k}). \tag{2}$$

Here τ_x is one Pauli matrix in Nambu space, and $\Delta(\mathbf{k})$ is a 6×6 matrix. Our purpose is to identify the exact form of $\Delta(\mathbf{k})$. For convenience, we utilize four Pauli matrices (s_0,s_x,s_y,s_z) to span spin space and nine Gell-Mann matrices $(\lambda_0,\ldots,\lambda_8)$ (see Appendix B for definitions of Gell-Mann matrices) to span orbital space. In such a way, $\Delta(\mathbf{k})$ can be decomposed into the product of the Pauli matrices and Gell-Mann matrices, i.e., $\Delta(\mathbf{k})=f(\mathbf{k})s_m\lambda_n$, in which $f(\mathbf{k})$ is the pairing form factor. We summarize all the possibilities of the $(\mathbf{k},-\mathbf{k})$ on-site pairing channels according to the IRs of D_{4h} in Table I and non-on-site pairing channels up to the next-nearest neighbor in Table II.

TABLE I. The IRs of all the possible on-site superconducting pairing in $(\mathbf{k},-\mathbf{k})$ channels. Here $\eta_{1/4}=\mp\frac{1}{3}(\lambda_0+2\sqrt{3}\lambda_8)$ and $\eta_{2/3}=\frac{1}{3}(\mp\lambda_0\pm\sqrt{3}\lambda_8\mp 3\lambda_{3/1})$.

$(\mathbf{k},-\mathbf{k})$: $\Delta(\mathbf{k})$	$c_2(z)$	$c_2(x)$	σ_d	$\{i\vert\frac{1}{2}\frac{1}{2}\}$	IR
	$-is_z\eta_1$	$-is_x\eta_2$	$\frac{-i(s_x-s_y)\eta_3}{\sqrt{2}}$	$s_0\eta_4$	
$s_0\lambda_0$	1	1	1	1	$A_{1g}^{(1)}$
$s_0\lambda_8$	1	1	1	1	A_{1g}
$s_0\lambda_1$	1	-1	1	1	B_{2g}
$s_0(\lambda_4,\lambda_6)$	$(-1,-1)$	$(1,-1)$	$s_0(\lambda_6,\lambda_4)$	$(-1,-1)$	E_u
$is_z\lambda_2$	1	1	1	1	A_{1g}
$s_z(\lambda_5,\lambda_7)$	$(-1,-1)$	$(-1,1)$	$-s_z(\lambda_7,\lambda_5)$	$(-1,-1)$	$E_u^{(1)}$
$i(s_x,s_y)\lambda_2$	$(-1,-1)$	$(-1,1)$	$i(s_y,s_x)\lambda_2$	(1,1)	E_g
$i(s_x\lambda_5,s_y\lambda_7)$	(1,1)	(1,1)	$-i(s_y\lambda_7,s_x\lambda_5)$	$(-1,-1)$	$E_u^{(2)}$
$i(s_y\lambda_5,s_x\lambda_7)$	(1,1)	$(-1,-1)$	$-i(s_x\lambda_7,s_y\lambda_5)$	$(-1,-1)$	$E_u^{(2')}$

TABLE II. The IRs of all the possible nearest and next-nearest neighbor superconducting pairing in $(\mathbf{k},-\mathbf{k})$ channels. Here $f_{1/2}(k)=\cos k_x\pm\cos k_y$; $f_4(k)=\cos k_x\cos k_y$; $[f_3(k_x),f_3(k_y)]=[\sin k_x,\sin k_y]$; $f_5(k)=\sin k_x\sin k_y$.

$(\mathbf{k},-\mathbf{k})$: $\Delta(\mathbf{k})$	IR
$f_{1/4}(k)s_0\lambda_{0/8},f_5(k)s_0\lambda_1,f_3(k_x)s_0\lambda_5+f_3(k_y)s_0\lambda_7$	$A_{1g}^{(2)}$
$f_2(k)s_0\lambda_{0/8},f_3(k_x)s_0\lambda_5-f_3(k_y)s_0\lambda_7$	$B_{1g}^{(1)}$
$f_2(k)s_0\lambda_1,f_3(k_y)s_0\lambda_5-f_3(k_x)s_0\lambda_7$	A_{2g}
$f_5(k)s_0\lambda_{0/8},f_{1/4}(k)s_0\lambda_1,f_3(k_y)s_0\lambda_5+f_3(k_x)s_0\lambda_7$	B_{2g}
$if_{1/4}(k)s_z\lambda_2,i^{1/0/0}[f_3(k_x)s_{z/x/y}\lambda_4+if_3(k_y)s_{z/y/x}\lambda_6]$	A_{1g}
$if_2(k)s_z\lambda_2,i^{1/0/0}[f_3(k_x)s_{z/x/y}\lambda_4-if_3(k_y)s_{z/y/x}\lambda_6]$	B_{1g}
$i^{1/0/0}[f_3(k_y)s_{z/x/y}\lambda_4-f_3(k_x)s_{z/y/x}\lambda_6]$	A_{2g}
$if_5(k)s_z\lambda_2,i^{1/0/0}[f_3(k_y)s_{z/x/y}\lambda_4+f_3(k_x)s_{z/y/x}\lambda_6]$	B_{2g}
$if_{1/2/4/5}(k)(s_x,s_y)\lambda_2$	E_g
$f_3(k_x)s_{x/y}\lambda_0\pm f_3(k_y)s_{y/x}\lambda_0$	$A_{1u}^{(1)}$
$[f_3(k_x),f_3(k_y)]s_z\lambda_0$	$E_u^{(3)}$

In both Tables I and II the spin-singlet/spin-triplet pairing channels are listed in the first/second parts.

III. TOPOLOGICAL SUPERCONDUCTING STATES

To evaluate the pairing channels that could support the topological SC states, we first impose the nodeless gap structure restrictions to the pairing channels in Tables I and II according to ARPES and STM/S experimental results [9–11], i.e., $A_{1g}^{(1)}$, $E_u^{(1)}$, $E_u^{(2)}$, and $E_u^{(2')}$ in Table I and $A_{1g}^{(1)}$ with $f_4(k)s_0\lambda_0$, $B_{1g}^{(1)}$, $A_{1u}^{(1)}$, and $E_u^{(3)}$ in Table II. Second, we focus on the odd-parity pairing channels based on the proposals that odd-parity pairings usually support the topological SC states in doped topological insulators [4]. Finally, we consider the SC states with the C_4 rotation symmetry verified by both experimental observations [10–13] and our calculations in Sec. IV. This constraint forces the time-reversal (TR) symmetry to be broken spontaneously for some E_u states. With all the above constraints and a turn to the monolayer FeSe/STO, four possible odd-parity pairing states survive: (1) $E_u^{(1)}$, a doubly degenerate TR breaking state with $\Delta_1(\mathbf{k}) = \Delta_0 s_z(\lambda_5 \pm i\lambda_7)$, (2) $E_u^{(2)}$, a TR invariant state with $\Delta_2(\mathbf{k}) = \Delta_0 i(s_x\lambda_5 + s_y\lambda_7)$ (note that $E_u^{(2')}$ is equivalent to $E_u^{(2)}$), (3) $E_u^{(3)}$, a doubly degenerate TR breaking state with $\Delta_3(\mathbf{k}) = \Delta_0[f_3(k_x) \pm i f_3(k_y)]s_z\lambda_0$, and (4) $A_{1u}^{(1)}$, a TR invariant state with $\Delta_4(\mathbf{k}) = \Delta_0[f_3(k_x)s_x\lambda_0 + f_3(k_y)s_y\lambda_0]$ [note that all four components in $\{A_{1u}^{(1)}\text{: } f_3(k_x)s_{x/y}\lambda_0 \pm f_3(k_y)s_{y/x}\lambda_0\}$ are equivalent]. Through the bulk-boundary correspondence, we demonstrate that all these four kinds of odd-parity pairing channels support topological SC states in monolayer FeSe/STO. The BdG Hamiltonian describing the SC states can be obtained by combining the tight-binding Hamiltonian H_0 in Eq. (1) and pairing term H_p in Eq. (2), i.e.,

$$H_{\mathrm{BdG}} = H_0 + H_p. \tag{3}$$

Note that H_{BdG} in Eq. (3) includes both odd-orbital-parity and even-orbital-parity parts. The edge spectra from the odd-orbital-parity parts of H_{BdG} with $\Delta_1(\mathbf{k})\cdots\Delta_4(\mathbf{k})$ are presented in Fig. 2. The even-orbital-parity parts of H_{BdG} give the same spectra if k_y is translated to $k_y + \pi$ [see Fig. 1(b) for comparison]. The edge spectra in Fig. 2 explicitly support the Andreev bound states which are the identifications of topological superconductors. Besides, the bulk properties of topological superconductors are usually characterized by some topological numbers. Here the pairing channels with $\Delta_1(\mathbf{k})$ and $\Delta_3(\mathbf{k})$ break the TR symmetry, and the Chern number [29] can be introduced to characterize such two states, i.e., $\mathcal{C} = \frac{i}{2\pi}\sum_{E_n<0}\int_{\mathrm{BZ}} d\mathbf{k}\langle\nabla_k u_n(\mathbf{k})| \times |\nabla_k u_n(\mathbf{k})\rangle$. The calculations show that both odd-orbital-parity and even-orbital-parity parts give the Chern numbers $\mathcal{C}^o = \mathcal{C}^e = 4$ in the one-Fe BZ for $\Delta_1(\mathbf{k})$ and $\Delta_3(\mathbf{k})$ pairing channels. Thus, two such pairing channels are characterized by the total Chern number $\mathcal{C} = \frac{1}{2}(\mathcal{C}^o + \mathcal{C}^e) = 4$ in the two-Fe BZ. The Chern number $\mathcal{C} = 4$ is equal to the number of edge Andreev bound states shown in Figs. 2(a) and 2(d). For the TR invariant $\Delta_2(\mathbf{k})$ and $\Delta_4(\mathbf{k})$ pairing channels, the total Chern numbers are zero. However, the spin Chern numbers [30,31] can be introduced to characterize the bulk topological properties of SC states in $\Delta_2(\mathbf{k})$ or $\Delta_4(\mathbf{k})$ pairing channels. Namely,

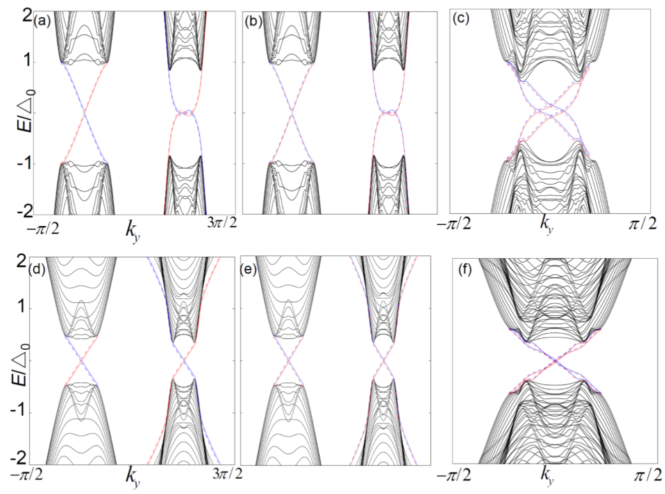

FIG. 2. (Color online) The edge spectra of odd-orbital-parity BdG Hamiltonian with $\Delta_1(k)$, $\Delta_2(k)$, $\Delta_3(k)$, and $\Delta_4(k)$ in (a), (b), (d), and (e). In the presence of the orbital-parity-broken perturbation, i.e., the staggered potential of Fe sublattices, the edge spectra of BdG Hamiltonian with $\Delta_2(k)$ and $\Delta_4(k)$ are shown in (c) and (f). Here the system has a periodic boundary condition along the y direction and an open boundary condition along the x direction with 51 one-Fe unit cell lengths. The red/blue colors label the edge states localizing at the opposite boundaries, and the dashed/solid lines label the edge states with up/down spin directions. Note that the degenerate edge states on the same edge are artificially split as a guide for the eye.

$\mathcal{C}_\uparrow^{o/e} = 1$, $\mathcal{C}_\downarrow^{o/e} = -1$ in the two-Fe BZ. Correspondingly, two Z_2 topological numbers [32] with opposite orbital parities defined by $\upsilon^{o/e} = \frac{1}{2}(\mathcal{C}_\uparrow^{o/e} - \mathcal{C}_\downarrow^{o/e}) = 1$ characterize the bulk topological properties for SC states in $\Delta_2(\mathbf{k})$ or $\Delta_4(\mathbf{k})$ pairing channels.

Having confirmed that the topological SC states emerge in the nodeless odd-parity pairing channels, we notice that the edge spectra shown in Figs. 2(a) and 2(b) and the edge spectra shown in Figs. 2(d) and 2(e) are very different. Therefore, it is necessary to extract the minimum effective models to clarify the essential physics hidden behind. First, we are aware of the $\Delta_{3/4}(\mathbf{k})$ pairing channels being in the intraorbital spin-triplet p-wave pairing channels. Thus, the orbital degree of freedom is inessential, and the minimum effective Hamiltonian can be reduced into the single band space, which is the same Hamiltonian to describe the well-known $p \pm ip$ topological superconductors/superfluids [1,33,34], and the nontrivial topology is referred to the $p \pm ip$ pairing terms. Therefore, we omit our discussions for these "trivial" topological SC states.

For $\Delta_1(\mathbf{k})$ and $\Delta_2(\mathbf{k})$, which are the interorbital spin-triplet s-wave pairing channels, the three t_{2g} orbitals are involved and entangled with each other not only in the bands around the Fermi surface shown in Fig. 3(a), but in the pairing terms shown in Fig. 3(d). Note that we should have three bands when we consider three t_{2g} orbitals. It indicates that the third band mainly with the d_{xz} and d_{yz} weight has to strongly couple with two e_g orbitals and be gapped and pushed away from the Fermi level. In order to describe the two bands in an exact three orbital basis, we adopt the angular momentum representation characterized by the azimuthal

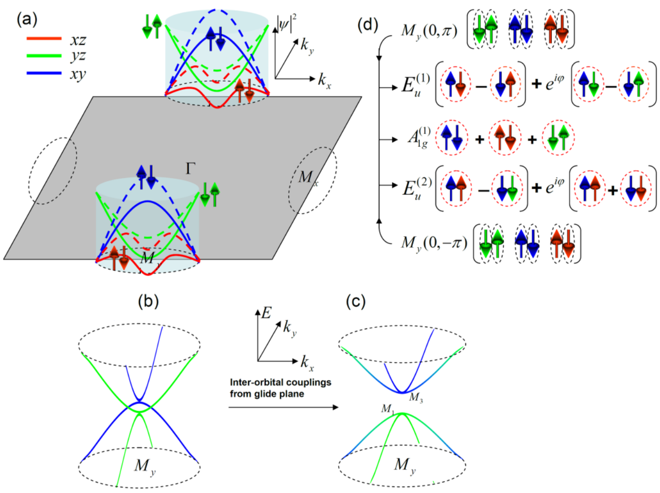

FIG. 3. (Color online) (a) The weight of three t_{2g} along the Fermi surface around M_y with odd-orbital parity. (b) and (c) The effective band dispersions without/with interorbital coupling from the glide plane. (d) Three competitive pairing channels with $\varphi = \frac{\pi}{2}$ in weak-coupling limit.

and magnetic quantum numbers l and m. The new electron creation operators are $d^{\dagger}_{(lm=2,\pm1),\sigma}(\mathbf{k}) = \mp\frac{1}{\sqrt{2}}[d^{\dagger}_{xz,\sigma}(\mathbf{k}) \pm id^{\dagger}_{yz,\sigma}(\mathbf{k})]$, then we have $\hat{\Delta}^{\dagger}_1(\mathbf{k}) \sim [d^{\dagger}_{(2,1),\uparrow}(\mathbf{k})d^{\dagger}_{xy,\downarrow}(-\mathbf{k}) + d^{\dagger}_{(2,1),\downarrow}(\mathbf{k})d^{\dagger}_{xy,\uparrow}(-\mathbf{k})]$ and $\hat{\Delta}^{\dagger}_2(\mathbf{k}) \sim [d^{\dagger}_{(2,-1),\uparrow}(\mathbf{k})d^{\dagger}_{xy,\uparrow}(-\mathbf{k}) + d^{\dagger}_{(2,1),\downarrow}(\mathbf{k})d^{\dagger}_{xy,\downarrow}(-\mathbf{k})]$. Now we can only exploit the operators involved in $\hat{\Delta}_{1/2}(\mathbf{k})$ to construct the basis to write the minimum effective Hamiltonian, and this approximation is equivalent to treating d_{xz} and d_{yz} orbitals with equal weights. In the effective basis, $\Psi_{1/2}(\mathbf{k}) = [\{\psi_{1/2\uparrow}(\mathbf{k})\},\{\psi_{1/2\downarrow}(\mathbf{k})\}]^T$ with $\{\psi_{1/2,\sigma}(\mathbf{k})\} = \{d_{[2,1/-(-1)^{\sigma}],\sigma}(\mathbf{k}), d_{xy,\sigma}(\mathbf{k}), d^{\dagger}_{xy,\bar{\sigma}/\sigma}(-\mathbf{k}), -d^{\dagger}_{[2,1/-(-1)^{\sigma}]\bar{\sigma}}(-\mathbf{k})\}$,

$$H^{(1/2)}(\mathbf{k}) = \mathcal{H}^{(1/2)}_1(\mathbf{k}) \oplus \mathcal{H}^{(1/2)}_2(\mathbf{k}). \quad (4)$$

Here $\mathbf{k}$ is measured from the M point. $\bar{\sigma} = -\sigma$ and $(-1)^{\sigma} = 1/-1$ for spin $\downarrow/\uparrow$, the orbital parity index is omitted for simplicity. $\mathcal{H}^{(1/2)}_1(\mathbf{k}) = \tau_z[d^{(1/2)}_0(\mathbf{k}) + \sum_{i=x}^{z} d^{(1/2)}_i(\mathbf{k})\sigma_i] + \tau_x\Delta_0$, $\mathcal{H}^{(1)}_2(\mathbf{k}) = \mathcal{H}^{(1)}_1(\mathbf{k})$ and $\mathcal{H}^{(2)}_2(\mathbf{k}) = \mathcal{H}^{(2)*}_1(-\mathbf{k})$. The three Pauli matrices $\sigma_{1/2/3}$ are introduced to span the effective two-band space. $d^{(1/2)}_0(\mathbf{k}) = \frac{\varepsilon_1(\mathbf{k})+\varepsilon_2(\mathbf{k})}{2} - \mu$, $d^{(1/2)}_x(\mathbf{k}) = \mp Ak_y$, $d^{(1/2)}_y(\mathbf{k}) = -Ak_x$, and $d^{(1/2)}_z(\mathbf{k}) = \frac{\varepsilon_1(\mathbf{k})-\varepsilon_2(\mathbf{k})}{2}$. $H^{(1)}(\mathbf{k})$ breaks TR symmetry, because only $m = 1$ is involved. $H^{(2)}(\mathbf{k})$ is TR invariant, and characterized by the $T^{-1}H^{(2)}(\mathbf{k})T = H^{(2)^*}(-\mathbf{k})$, where the TR symmetry operator is $T = is_y\tau_0\sigma_0\mathcal{K}$ with $\mathcal{K}$ the complex conjugated operator. The dispersions $\varepsilon_{1/2}(\mathbf{k})$ with definite orbital parity can be read out from Figs. 1(e) and 3(b). Around M_y point, we have $\varepsilon^e_{1/2}(\mathbf{k}) = e_{1/2} - \mu + \alpha_{1/2}k_x^2 + \beta_{1/2}k_y^2$ and $\varepsilon^o_{1/2}(\mathbf{k}) = e_{1/2} - \mu + \beta_{1/2}k_x^2 + \alpha_{1/2}k_y^2$. The signs of α/β are crucial to determine the properties of the topological SC states. In Figs. 3(b) and 3(c) we schematically illustrate the evolution of the $\varepsilon^o_{1/2}(\mathbf{k})$ under the couplings induced by the glide plane around M_y point, and we can find $e_1 < e_2, \alpha_1 < 0, \beta_1 > 0, \alpha_2 > 0, \beta_2 < 0$. The effective mass measuring the energy gap $E_{M_3} - E_{M_1}$ shown in Fig. 1(e) or 3 (c) is $m = \frac{e_2-e_1}{2} > 0$. The finite electron-doped condition $\mu^2 + \Delta_0^2 > m^2$ [35] always supports topological SC states for $\mathcal{H}^{(1/2)}_1(\mathbf{k})$, where the chemical potential μ is measured from the middle of the gap. The remarkable feature of the edge spectra in Figs. 2(a) and 2(b) is that the edge Andreev bound states have a twist (three times of crossings) around $k_y = \pi$ and only one crossing around $k_y = 0$. This difference can be understood with the "orbital mirror helicity" from the mirror operator in $c_2(x/y)$ acting on three t_{2g} orbitals in analogy to the "spin mirror helicity" proposed in Ref. [35]. The conservation of mirror helicity force the nontwisted/twisted feature of the edge Andreev edge states under the nonband/band-inversion conditions between $\varepsilon^{e/o}_1(\mathbf{k})$ and $\varepsilon^{e/o}_2(\mathbf{k})$ along the x direction, sgn$[(e_2 - e_1)(\alpha_2 - \alpha_1)] > 0$/sgn$[(e_2 - e_1)(\beta_2 - \beta_1)] < 0$ [note that $\varepsilon^e_{1/2}(\mathbf{M}_y + \mathbf{k}) = \varepsilon^o_{1/2}(\mathbf{M}_x + \mathbf{k})$]. We are aware of the importance of the nonsymmorphic lattice symmetry which not only induces the orbital-momentum locking $\mathbf{k} \times \sigma \cdot \hat{\mathbf{z}}$ through the glide plane, but protects the exotic behaviors of the edge Andreev bound states. We can verify this point through introducing the staggered on-site potential, which mixes the orbital parities, breaks the nonsymmorphic lattice symmetry, and destroys the twist feature of the edge spectra. The results are shown in Figs. 2(c) and 2(f). However, the bulk topological properties are robust against such perturbations.

IV. THE EFFECTIVE PAIRING INTERACTIONS

Although the high temperature interfacial superconductivity in monolayer FeSe/STO seems to have been established beyond doubt, the mechanism for superconductivity is still an open question [36], and the unique features of monolayer FeSe/STO further pose a higher barrier to block our understanding of the superconductivity from some standard theories. For example, the monolayer FeSe/STO is strictly two dimensional and has no hole pockets at the BZ center, while its three-dimensional counterpart bulk FeSe resembles iron-pnictide with hole pockets. The Fermi surface of monolayer FeSe/STO is similar to that of $A_xFe_{2-y}Se_2$ (A = K, Cs, Rb), except that the small electron pocket around $(0,0,\pi)$ in $A_xFe_{2-y}Se_2$ is absent here. In weak coupling limit, the spin-fluctuation-exchange theory predicts that the $\{B_{1g}$: $f_2(k)s_0\lambda_0\}$ pairing channel is dominant in $A_xFe_{2-y}Se_2$ and the gap structure has nodes along the k_z direction [37,38]. However, the ARPES measurements reported isotropic full gaps without nodes on all pockets in $A_xFe_{2-y}Se_2$ [39,40]. In the strong coupling limit, the phenomenological t-J model predicts that the $\{A_{1g}$: $f_4(k)s_0\lambda_0\}$ pairing channel is dominant in $A_xFe_{2-y}Se_2$ and the gaps have same sign for all the pockets [41]. However, the inelastic neutron scattering measurements on $A_xFe_{2-y}Se_2$ reported a resonance with wave vector $\mathbf{Q}_c = (\pi,\pi/2)$ in the superconducting state [42], which indicated that there existed a sign change between the Fermi surfaces connected by $\mathbf{Q}_c$. These contradictions strongly question the standard theories. On the other hand, the studies of some confirmed systems with interfacial superconductivity including bilayer lanthanum cuprate [43] and $LaAlO_3/SrTiO_3$ heterostructure [44] could provide us some useful insights to understand the superconductivity in monolayer FeSe/STO. The studies of the aforementioned systems indicate that surface phonon plays a key role to drive the superconductivity [45]. A recent ARPES experiment observed the band replication, which was attributed to strong coupling between the cross phonon and electrons [15], and the cooperation between the cross phonon mode and spin fluctuation is argued to be the origin to enhance T_c in monolayer FeSe/STO. Therefore, it is still possible that the superconductivity in monolayer FeSe/STO is driven by the electron-phonon coupling, and the surface phonon-mediated SC mechanism in monolayer FeSe/STO has been proposed in Ref. [46]. Here, without loss of generality, we consider several possibilities of the effective interactions that can drive superconductivity in different pairing channels and focus on the parameter regime missed previously.

We first assume the multiorbital Hubbard interactions as a pairing driver,

$$H_{\rm int}^{(1)} = U\sum_{i,l} n_{il\uparrow}n_{il\downarrow} + V\sum_{i,l>l'} n_{il}n_{il'} + J_H\sum_{i,l>l'}\left(2\mathbf{S}_{il}\cdot\mathbf{S}_{il'} + \frac{1}{2}n_{il}n_{il'}\right) + J'\sum_{i,l\neq l'} d^\dagger_{i,l\uparrow}d^\dagger_{i,l\downarrow}d_{i,l'\downarrow}d_{i,l'\uparrow}. \quad (5)$$

Here U, V, J_H, J' are the intraorbital, interorbital, Hund's coupling, and pairing hopping term. $l,l' \in (xz,yz,xy)$, and $\mathbf{S}_{il} = \frac{1}{2}d^\dagger_{il\sigma}\mathbf{s}_{\sigma\sigma'}d_{il\sigma}$. The spin rotation symmetry requires $U = V + 2J_H$, and $J_H = J'$ at the atomic level. Since the predictions from the weak-coupling theory [37,38] about $H_0 + H_{\rm int}^{(1)}$ were not consistent with the experimental reports [39,40], the strongly correlative picture with quite large J_H is possible and the strongly correlative effects in iron chalcogenides have been reported by recent ARPES experiments [47]. Define the pairing operators

$$\hat{\Delta}_{s,ll'} = \sum_k \hat{\Delta}_{s,ll'}(k), \quad \hat{\Delta}^\alpha_{t,ll'} = \sum_k \hat{\Delta}^\alpha_{t,ll'}(k),$$
$$\hat{\Delta}_{s,ll'}(k) = \sum_{\sigma\sigma'}\frac{[is_y]_{\sigma\sigma'}}{4}[d_{l\sigma}(\mathbf{k})d_{l'\sigma'}(-\mathbf{k}) + d_{l'\sigma}(\mathbf{k})d_{l\sigma'}(-\mathbf{k})],$$
$$\hat{\Delta}^\alpha_{t,ll'}(k) = \sum_{\sigma\sigma'}\frac{[is_ys_\alpha]_{\sigma\sigma'}}{4}[d_{l\sigma}(\mathbf{k})d_{l'\sigma'}(-\mathbf{k}) - d_{l'\sigma}(\mathbf{k})d_{l\sigma'}(-\mathbf{k})]. \quad (6)$$

The interaction Hamiltonian has the form

$$H_{\rm int}^{(1)} = U\sum_l \hat{\Delta}^\dagger_{s,ll}\hat{\Delta}_{s,ll} + J_H\sum_{l\neq l'}\hat{\Delta}^\dagger_{s,ll}\hat{\Delta}_{s,l'l'} + (V - J_H)\sum_{ll'\alpha}\hat{\Delta}^{\alpha\dagger}_{t,ll'}\hat{\Delta}^\alpha_{t,ll'} + (V + J_H)\sum_{l\neq l'}\hat{\Delta}^\dagger_{s,ll'}\hat{\Delta}_{s,ll'}. \quad (7)$$

When the Hund's coupling is strong enough, i.e., $J_H > U/3$, the third term of Eq. (7) can give rise to the instability in a spin-triplet channel [48,49], which involves the $\{A_{1g}\colon is_z\lambda_2\}$, $E_u^{(1)}$, and $E_u^{(2)}$ IRs in Table I. The detailed discussions about these pairing channels are merged into the third kind of effective interaction in the following.

Another standard theory for the superconductivity is the phenomenological Heisenberg model in the strong coupling limit, we consider the effectively frustrated Heisenberg interaction [50] as the pairing force,

$$H_{\rm int}^{(2)} = J_1\sum_{l,\langle i,j\rangle}\mathbf{S}_{il}\cdot\mathbf{S}_{jl} + J_2\sum_{l,\langle\langle i,j\rangle\rangle}\mathbf{S}_{il}\cdot\mathbf{S}_{jl}. \quad (8)$$

Here $J_{1/2}$ are the nearest and next-nearest neighbor magnetic exchange couplings. A well-know result of $H_{\rm int}^{(2)}$ is that the magnetic ground state is checkerboard antiferromagnetic when $2J_2 < |J_1|$, and collinear antiferromagnetic when $2J_2 > |J_1|$. However, no Fermi surface reconstruction induced by spin density wave was observed in monolayer FeSe/STO but in mutlilayer FeSe/STO in ARPES experiments [12]. The recent first-principles calculations proposed that the magnetic order was strongly frustrated in monolayer FeSe/STO with $2J_2 \approx |J_1|$ [51]. Another issue is the sign of J_1. If both J_1 and J_2 are antiferromagnetic, the $\Delta_{3/4}(\mathbf{k})$ pairing channels are ruled out, and the SC states fall into $\{A_{1g}\colon f_4(k)s_0\lambda_0\}$ induced by J_2 or $\{B_{1g}\colon f_2(k)s_0\lambda_0\}$ induced by J_1. If J_1 is ferromagnetic and J_2 are antiferromagnetic, the $\Delta_{3/4}(\mathbf{k})$ pairing channels are possible from the symmetry point, but these two odd-parity pairing channels have to compete with the $\{A_{1g}\colon f_4(k)s_0\lambda_0\}$ induced by J_2. The winner is determined by the topology of the Fermi surface [52]. For the low electron doped at $0.1e$/Fe, the Fermi pockets locating at M points are quite small. Therefore, the form factor $f_4(k)$ has large magnitude, and the SC states favor the $\{A_{1g}\colon f_4(k)s_0\lambda_0\}$. If the electron-doped level can be tuned in monolayer FeSe/STO without suppressing the superconductivity, we can expect that the SC states in over electron-doped samples would favor $\Delta_{3/4}(\mathbf{k})$ pairing channels for ferromagnetic J_1, because the Fermi surface locates at the X points, where the form factors $f_3(k_{x/y})$ have large magnitudes. We note that such kind of pairing was discussed in underdoped cuprates [53].

From the aforementioned arguments about the possibly significant role of surface phonon, we consider the third kind of phenomenological interaction to induce the interfacial SC instability in monolayer FeSe/STO,

$$H_{\rm int}^{(3)} = \sum_{l,l',\sigma,\sigma',\mathbf{k},\mathbf{k}'}\frac{1}{2}V^{\sigma,\sigma'}_{l,l'}(\mathbf{k},\mathbf{k}')d^\dagger_{k,l\sigma}d^\dagger_{-k,l'\sigma'}d_{-k'l'\sigma'}d_{k',l\sigma}. \quad (9)$$

Here we assume $V^{\sigma,\sigma'}_{l,l'}(\mathbf{k},\mathbf{k}') = -V_0$ for $l = l'$, $\sigma' = \bar{\sigma}$ and $V^{\sigma,\sigma'}_{l,l'}(\mathbf{k},\mathbf{k}') = -V_1$ for $l > l'$. Note that the third term in Eq. (7) with $J_H > U/3$ can also be described by $H_{\rm int}^{(3)}$. With the pairing operators shown in Eq. (6), $H_{\rm int}^{(3)}$ takes the form

$$H_{\rm int}^{(3)} = -V_0\sum_l \hat{\Delta}^\dagger_{s,ll}\hat{\Delta}_{s,ll} - V_1\sum_{l>l'}\hat{\Delta}^\dagger_{s,ll'}\hat{\Delta}_{s,ll'} - V_1\sum_{l>l'\alpha}\hat{\Delta}^{\alpha\dagger}_{t,ll'}\hat{\Delta}^\alpha_{t,ll'}. \quad (10)$$

Under the mean-field approximation $\Delta_{s,ll'} = \langle\hat{\Delta}^\dagger_{s,ll'}\rangle$, $\Delta^\alpha_{t,ll'} = \langle\hat{\Delta}^\alpha_{t,ll'}\rangle$, the $H_{\rm int}^{(3)}$ can be decoupled as follows:

$$H_{\rm int}^{(3)} = -V_0\sum_l \Delta_{s,ll}\hat{\Delta}^\dagger_{s,ll} - V_1\sum_{l>l'}\Delta_{s,ll'}\hat{\Delta}^\dagger_{s,ll'} - V_1\sum_{l>l'\alpha}\Delta^\alpha_{t,ll'}\hat{\Delta}^{\alpha\dagger}_{t,ll'} + \text{H.c.} + h_{\rm con}. \quad (11)$$

Here $h_{\text{con}} = \sum_l V_0|\Delta_{s,ll}|^2 + V_1\sum_{l>l'}|\Delta_{s,ll'}|^2 + V_1\sum_{l>l',\alpha}|\Delta^{\alpha}_{s,ll'}|^2$. Now we consider the odd-orbital-parity parts of the normal-state Hamiltonian. The mean-field Hamiltonian takes the following form:

$$H_{\text{MF}} = \sum_k \frac{1}{2}\Psi^{\dagger}(k)H_{\text{MF}}(k)\Psi(k) + H_{\text{con}}, \tag{12}$$

where $\Psi(k)$ has the same form shown in Eq. (2) except $\{d_\sigma(\mathbf{k})\} = \{d_{xz,\sigma}(\mathbf{k}), d_{yz,\sigma}(\mathbf{k}), d_{xy,\sigma}(\mathbf{k}), d_{x^2-y^2,\sigma}(\mathbf{k}), d_{z^2,\sigma}(\mathbf{k})\}$ now. Then $H_{\text{MF}}(k) = H_0(k)\tau_z + \Delta(k)\tau_x$, $H_0(k) = A_o(k)\oplus A_o(k)$, and $H_{\text{con}} = \sum_{k,m=1}^{5} A_{o,mm}(k) + h_{\text{con}}$. Assume the $H_{\text{MF}}(k)$ can be diagonalized with matrix $\tilde{U}_k$, i.e., $\tilde{U}_k^{\dagger}H_{\text{MF}}(k)\tilde{U}_k = E_{k,1}\oplus E_{k,2}\cdots E_{k,20}$. Then the mean-field self-consistent equations take the forms

$$\begin{aligned}
\Delta_{s,ll'} &= \sum_{k,n=1}^{20}\frac{[\tilde{U}^*_{k,n,l}\tilde{U}_{k,n,l'+10} + \tilde{U}^*_{k,n,l+5}\tilde{U}_{k,n,l'+15}]f(E_{k,n})}{2},\\
\Delta^{x}_{t,ll'} &= \sum_{k,n=1}^{20}\frac{-[\tilde{U}^*_{k,n,l}\tilde{U}_{k,n,l'+15} + \tilde{U}^*_{k,n,l+5}\tilde{U}_{k,n,l'+10}]f(E_{k,n})}{2},\\
\Delta^{y}_{t,ll'} &= \sum_{k,n=1}^{20}\frac{-i[\tilde{U}^*_{k,n,l}\tilde{U}_{k,n,l'+15} - \tilde{U}^*_{k,n,l+5}\tilde{U}_{k,n,l'+10}]f(E_{k,n})}{2},\\
\Delta^{z}_{t,ll'} &= \sum_{k,n=1}^{20}\frac{-[\tilde{U}^*_{k,n,l}\tilde{U}_{k,n,l'+10} - \tilde{U}^*_{k,n,l+5}\tilde{U}_{k,n,l'+10}]f(E_{k,n})}{2},\\
N_e &= \sum_{k,n=1}^{20}\sum_{m=1}^{10}|\tilde{U}^*_{k,n,m}|^2 f(E_{k,n}).
\end{aligned} \tag{13}$$

Here $f(x) = \frac{1}{e^{\frac{x}{k_BT}}+1}$ is the Fermi distribution function and N_e is the electron number. In comparison with Table I and Eq. (11), the relevant IR channels in Table I can be represented with (13). For example, $\{A^{(1)}_{1g}\colon s_0\lambda_0\} = s_0(\Delta_{s,xz,xz}\oplus\Delta_{s,yz,yz}\oplus\Delta_{s,xy,xy})$, $\{E^{(2)}_u\colon i(s_x\lambda_5,s_y\lambda_7)\} = i(\Delta^{x}_{t,xz,xy}s_x\lambda_5,\Delta^{y}_{t,xz,xy}s_y\lambda_7)$. Likewise, other IR channels can be read out following the same way.

It is possible for $\Delta(k)$ to take the form of linear combinations of several different IR channels, but some symmetries have to be broken to pay the price for such coexistence. For example the inverse symmetry is broken for the SC states proposed in Refs. [21,22]. Likewise, the TR symmetry or lattice symmetry could also be broken when two different one-dimensional IRs or two components in a two-dimensional IR coexist. In order to gain some insight before we perform the numerical calculations, we note that all the experiments reported the isotropic Fermi surface and gap structures without any resolvable distortions, and the monolayer FeSe/STO was conformed to be the cleanest composition with the simplest structure [10–12]. These features rule out the possibilities of some complex orders, such as nematic order found in bulk FeSe. From Table I we can first eliminate the possibilities of the $\{B_{2g}\colon s_0\lambda_1\}$, $\{A_{1g}\colon is_z\lambda_2\}$, $\{E_g\colon i(s_x,s_y)\lambda_2\}$, and $\{A_{1g}\colon s_0\lambda_8\}$ pairing channels, because the leading inter-d_{xz}-d_{yz} hopping term is proportional to $\sin k_x\sin k_y$, which is nearly zero around the Fermi surface, and the $\{A_{1g}\colon s_0\lambda_8\}$ channel has nodes. Second, it is straightforward to check that two components in $\{E_u\colon s_0(\lambda_4,\lambda_6)\}$ or $\{E^{(1)}_u\colon s_z(\lambda_5,\lambda_7)\}$ give two degenerate strip SC states with nodes. Thus, the TR-broken linear combination of two components is optimal to achieve the isotropic nodeless gap structure and lower the energy. Note that the coexistence of these two two-dimensional IRs could raise the energy, because they follow different transformations under the lattice symmetric operations and suppress the gap amplitude. Finally, no additionally global symmetries can be broken for $\{A^{(1)}_{1g}\colon s_0\lambda_0\}$ and $\{E^{(2)}_u\colon i(s_x\lambda_5,s_y\lambda_7)\}$ to coexist with each other and with $\{E_u\colon s_0(\lambda_4,\lambda_6)\}$ or $\{E^{(1)}_u\colon s_z(\lambda_5,\lambda_7)\}$ to avoid breaking the isotropic SC gap structure and achieving lower energy. Therefore, we find that these four IRs, i.e., $\{E_u\colon s_0(\lambda_4,\lambda_6)\}$, $\{E^{(1)}_u\colon s_z(\lambda_5,\lambda_7)\}$, $\{A^{(1)}_{1g}\colon s_0\lambda_0\}$, and $\{E^{(2)}_u\colon i(s_x\lambda_5,s_y\lambda_7)\}$ are independent, and TR symmetry should be spontaneously broken in the first two IRs. It is straightforward to verify these arguments through the following numerical calculations.

Now we perform the numerical calculations to evaluate which pairing channel governs the ground state of the system for different V_0 and V_1. The ground state energy of Eq. (12) is $G_s(T) = -k_BT\ln\text{Tr}e^{-\beta H_{\text{MF}}}$, and $G_s(T\sim 0) = (H_{\text{con}} - \frac{1}{2}\sum_{k,n=1}^{10}|E_{k,n}|)$ at zero temperature. For simplicity we can evaluate the ground state through the minimum of the condensed energy density defined as $f_g = h_{\text{con}} - \frac{1}{8\pi^2}\sum_{n=1}^{10}\int d^2\mathbf{k}|E_{k,n}| - \frac{1}{4\pi^2}\sum_{n=1}^{5}\int d^2\mathbf{k}|E^o_{k,n}|$ for given electron number, where $E^o_{k,n}$ are the energy spectra of normal state. Solve the self-consistent equations (12) and (13) for parameters (V_0,V_1) with respect to the minimum of f_g, we show the evolution of SC order parameters and condensed energy about (V_0,V_1) in Fig. 4, and we find topologically trivial $\{A^{(1)}_{1g}\colon s_0\lambda_0\}$ channel and topologically nontrivial

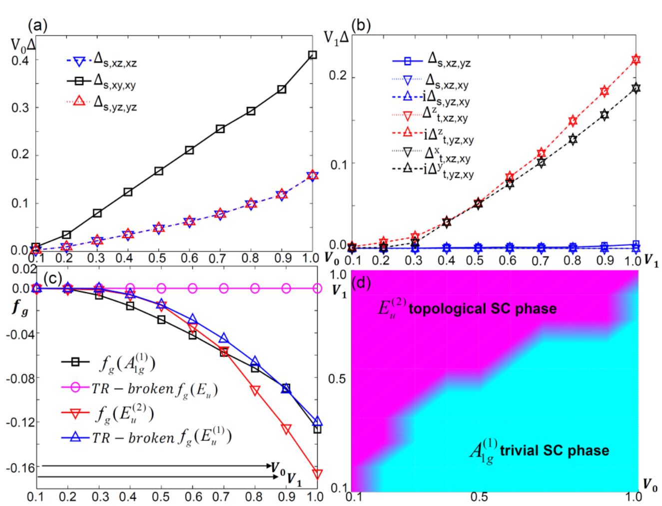

FIG. 4. (Color online) (a) The evolution of three components of SC order parameters in $A^{(1)}_{1g}$ channel about V_0. (b) The evolution of components of SC order parameters in E_u, $E^{(1)}_u$, and $E^{(2)}_u$ channels about V_1. (c) The evolution of the condensed energy in different SC states with relevant IRs about V_0 and V_1. (d) The phase diagram is plotted in (V_0, V_1) plane with respect to the lowest energy. We set a 51×51 mesh of $\mathbf{k}$, and the electron number to satisfy electron-doped $0.1e$/Fe. The energy scale is measured with eV.

$\{E_u^{(2)}: i(s_x\lambda_5, s_y\lambda_7)\}$ are dominant in relevant regime of (V_0, V_1) parameter plane.

V. DISCUSSION AND SUMMARY

If the superconductivity in monolayer FeSe/STO is driven by the effective interaction $H_{\text{int}}^{(3)}$ in Eq. (10), the observed isotropic and nodeless s-wave gap structures select both topologically trivial $A_{1g}^{(1)}$ $(s_0\lambda_0)$ and nontrivial $E_u^{(2)}$ $[\Delta_2(\mathbf{k})]$ as possible candidates. The essential difference lies in that the former one has even-parity and spin-singlet pairing while the latter one has odd-parity and spin-triplet pairing. Therefore, it is unambiguous to adopt the experiments which can directly distinguish the spin states and parities to pin down the possible candidate. Particularly, temperature dependence of the nuclear magnetic relaxation (NMR) rate can be utilized to distinguish the two different pairings. The well-known result is that the NMR rate has a Hebel-Slichter peak at the SC transition temperature for the even-parity and spin-singlet s-wave SC state [54]. However, the Hebel-Slichter peak could disappear with the antipeak behavior due to the unique spin, orbital, and momentum locking effect in topological SC states with odd parity as shown in Ref. [55]. The parity of the Cooper pair is characterized by the inverse operator $\{i|\frac{1}{2}\frac{1}{2}\}$. It indicates the odd-parity pairing has a sign change or phase shift of π between the top Se and and bottom Se layers along the c axis compared with the even-parity pairing. Thus, the standard magnetic-flux modulation of dc SC quantum interference devices (SQUIDS) measurements [4,56,57] provide another scheme to distinguish the odd- and even-parity pairings. On the other hand, some transport measurements can also be applied to detect the topological superconductors, such as the thermal Hall conductivity [58,59]. The challenge for such measurements is that the FeSe is very air sensitive, and the experimental measurements should be performed under the ultrahigh vacuum condition.

In the aforementioned discussions about the SC pairings, we assume that the glide plane symmetry is not broken. Actually, there exist some possible effects to break the glide plane symmetry. For example, the atomic spin-orbital coupling could have non-neglectable effect in iron chalcogenides. It is explicit that the interorbital spin-orbital coupling can mix the bands with inverse orbital parities, and induce the interorbital SC pairing in $(\mathbf{k},-\mathbf{k}+\mathbf{Q})$ channels. However, the weight of inter-d_{xz}-d_{xy} spin-orbital coupling is proportional to $\lambda_{\text{so}} \sim 0.05$ eV [38], while the inter-d_{xz}-d_{xy} orbital hopping term with definite orbital parity is proportional to $|2it_x^{14}\sin k_F| \sim 0.3$ eV at the Fermi surface. We can estimate that the ratio between the amplitudes of SC pairing order parameter in $(\mathbf{k},-\mathbf{k}+\mathbf{Q})$ channel and that in $(\mathbf{k},-\mathbf{k})$ channel should be $\sim$0.025. It is straightforward to check that the coexistence of the SC pairings in $(\mathbf{k},-\mathbf{k})$ and $(\mathbf{k},-\mathbf{k}+\mathbf{Q})$ channels does not change the topological natures of the SC states with $E_u^{(1)}$ and $E_u^{(2)}$ IRs under the condition that the pairings in $(\mathbf{k},-\mathbf{k}+\mathbf{Q})$ channels have the reasonable amplitudes in the physical regime. The reason lies in that the pairings in the $(\mathbf{k},-\mathbf{k}+\mathbf{Q})$ channel correspond to the interband pairings in the band basis, and cannot drive the gap-closing-reopening process to achieve the quantum phase transition. Another issue should be noticed that the spin quantum number is adopted to label the SC pairings in the pairing classification, and such an approach is not exact when atomic spin-orbital coupling is involved. However, the approximation works well, because the atomic spin-orbital coupling here is quite small. Indeed, it is shown that the atomic spin-orbital coupling plays a secondary role in SC states in $A_xFe_{2-y}Se_2$ [38]. Other issues, such as the coupling between the monolayer FeSe and substrate STO, could also break the glide plane symmetry. Such couplings are tunable and strongly affected by the fabrication process and the substrate materials [13,60]. Here we consider the case that the strength of coupling between the monolayer FeSe and substrate is weak in comparison with the relevant hopping amplitude.

Compared with the general topological materials, in which the extended s and p orbitals are the bricks to build low-energy electronic structures, and the spin-orbital coupling plays an essential role in inducing the strong linear couplings, the linear couplings in monolayer FeSe/STO is attributed to effective couplings between $3d$ orbitals induced by d-p hybridizations from the unique nonsymmorphic lattice structures. Such features provide us an alternative route to search for the new topological materials in strongly correlated electron systems.

In conclusion, we propose that the monolayer FeSe/STO could support the odd-parity topological SC states with the nodeless s-wave gap structures. In contrast with other topological superconductors [2,4] in which the spin-orbital coupling plays a key role, such topological SC states have strong relations with the unique nonsymmorphic lattice symmetry which induces the orbital-momentum locking. Furthermore, we calculate the phase diagram and suggest some experimental schemes to identify such uniquely nontrivial topological SC states.

ACKNOWLEDGMENTS

We thank Professor J. P. Hu for helpful discussions. This work is supported by the Research Grant Council of Hong Kong under Grant No. HKU703713P.

APPENDIX A: THE TIGHT-BINDING HAMILTONIAN FROM SYMMETRY ANALYSES

In this Appendix we discuss the properties of the tight-binding Hamiltonian from the symmetric point. The trilayer structure of the monolayer FeSe is shown in Fig. 1 (see main text). We focus on the three space group operations including glide plane symmetry operator $\hat{g}_z = \{m_z|\mathbf{r}_0\}$ with $\mathbf{r}_0 = (\frac{1}{2}\frac{1}{2})$ and two reflection symmetry operations $\hat{g}_x = \{m_x|\mathbf{r}_0\}$ and $\hat{g}_{x'} = \{m_{x'}|00\}$. Besides, the lattice has inverse symmetry denoted by the operator $\hat{g}_i = \{i|\mathbf{r}_0\}$. According to the LDA calculation, we can only focus on Fe atoms, the Bloch wave functions for the $3d$ orbitals of Fe are defined as

$$|\alpha\eta,\mathbf{k}'\rangle = \frac{1}{\sqrt{N}}\sum_n e^{i\mathbf{k}'\cdot\mathbf{r}'_{n\eta}}\phi_\alpha(\mathbf{r}'-\mathbf{r}'_{n\eta}). \tag{A1}$$

Here $\mathbf{r}'_{n\eta} = \mathbf{R}'_n + \mathbf{r}'_\eta$ with lattice vector $\mathbf{R}'_n$ and the position $\mathbf{r}'_\eta$ of Fe atom $\eta = A,B$, and ϕ_α denotes the d orbital basis function ($\alpha = xz,yz,x^2-y^2,xy,z^2$). The symmetry operators acting on the basis function $|\alpha\eta,\mathbf{k}'\rangle$ have the following properties:

$$\hat{g}_{x'}|\alpha\eta,\mathbf{k}'\rangle = \sum_{\beta} m_{x',\alpha\beta}|\beta\eta,m_{x'}\mathbf{k}'\rangle,$$
$$\hat{g}_{z}|\alpha\eta,\mathbf{k}'\rangle = \sum_{\beta} e^{-i(\hat{m}_z\mathbf{k}')\cdot\mathbf{r}_0} m_{z,\alpha\beta}|\beta\bar{\eta},\hat{m}_z\mathbf{k}'\rangle, \quad (A2)$$
$$\hat{g}_{x}|\alpha\eta,\mathbf{k}'\rangle = \sum_{\beta} e^{-i(\hat{m}_x\mathbf{k}')\cdot\mathbf{r}_0} m_{x,\alpha\beta}|\beta\bar{\eta},\hat{m}_x\mathbf{k}'\rangle.$$

The relevant tight-binding (TB) Hamiltonian can be expressed as

$$H_0 = \sum_{\mathbf{k}'} \Psi^\dagger(\mathbf{k}')H(\mathbf{k}')\Psi(\mathbf{k}'), \quad (A3)$$

with

$$\Psi^\dagger(\mathbf{k}') = [\psi_A^\dagger(\mathbf{k}'),\psi_B^\dagger(\mathbf{k}')],$$
$$\psi_\eta^\dagger(\mathbf{k}') = [d^\dagger_{\eta,xz}(\mathbf{k}'),d^\dagger_{\eta,yz}(\mathbf{k}'),d^\dagger_{\eta,x^2-y^2}(\mathbf{k}'),d^\dagger_{\eta,xy}(\mathbf{k}'),d^\dagger_{\eta,z^2}(\mathbf{k}')]. \quad (A4)$$

In the basis $\Psi(\vec{k}')$, the corresponding transformation matrices for the three operations $\hat{g}_\alpha$ have the following forms:

$$U(\hat{g}_{x'}) = \begin{bmatrix} m_{x'} & 0 \\ 0 & m_{x'} \end{bmatrix},$$
$$U(\hat{g}_{z}) = \begin{bmatrix} 0 & e^{-i(m_z\mathbf{k}')\cdot\mathbf{r}_0}m_z \\ e^{-i(m_z\mathbf{k}')\cdot\mathbf{r}_0}m_z & 0 \end{bmatrix}, \quad (A5)$$
$$U(\hat{g}_{x}) = \begin{bmatrix} 0 & e^{-i(m_x\mathbf{k}')\cdot\mathbf{r}_0}m_x \\ e^{-i(m_z\mathbf{k}')\cdot\mathbf{r}_0}m_x & 0 \end{bmatrix},$$

where

$$m_{x'} = \begin{bmatrix} 0 & 1 & 0 & 0 & 0 \\ 1 & 0 & 0 & 0 & 0 \\ 0 & 0 & -1 & 0 & 0 \\ 0 & 0 & 0 & 1 & 0 \\ 0 & 0 & 0 & 0 & 1 \end{bmatrix},$$
$$m_{z} = \begin{bmatrix} -1 & 0 & 0 & 0 & 0 \\ 0 & -1 & 0 & 0 & 0 \\ 0 & 0 & 1 & 0 & 0 \\ 0 & 0 & 0 & 1 & 0 \\ 0 & 0 & 0 & 0 & 1 \end{bmatrix}, \quad (A6)$$
$$m_{x} = \begin{bmatrix} -1 & 0 & 0 & 0 & 0 \\ 0 & 1 & 0 & 0 & 0 \\ 0 & 0 & 1 & 0 & 0 \\ 0 & 0 & 0 & -1 & 0 \\ 0 & 0 & 0 & 0 & 1 \end{bmatrix}.$$

The symmetry of the Hamiltonian requires

$$H_0(\mathbf{k}') = U(\mathbf{k}')H_0(U\mathbf{k}')U^\dagger(\mathbf{k}'). \quad (A7)$$

Define

$$H_0(\mathbf{k}') = \begin{bmatrix} H_A(\mathbf{k}') & H_{AB}(\mathbf{k}') \\ H_{BA}(\mathbf{k}') & H_B(\mathbf{k}') \end{bmatrix}. \quad (A8)$$

We can get

$$H_{A/B}(k_{x'},k_{y'}) = m_{x'}H_{A/B}(-k_{x'},k_{y'})m_{x'},$$
$$H_{AB}(k_{x'},k_{y'}) = m_{x'}H_{AB}(-k_{x'},k_{y'})m_{x'}, \quad (A9)$$
$$H_{A}(k_{x'},k_{y'}) = m_z H_B(k_{x'},k_{y'})m_z,$$
$$H_{AB}(k_{x'},k_{y'}) = m_z H_{BA}(k_{x'},k_{y'})m_z, \quad (A10)$$
$$H_{A}(k_{x'},k_{y'}) = m_x H_B(-k_{y'},-k_{x'})m_x,$$
$$H_{AB}(k_{x'},k_{y'}) = m_x H_{BA}(-k_{y'},-k_{x'})m_x. \quad (A11)$$

Moreover, since $|\alpha\eta,\mathbf{k}'+\mathbf{G}'\rangle = e^{i\mathbf{G}'\cdot\mathbf{r}'_\eta}|\alpha\eta,\mathbf{k}'\rangle$,

$$H_{A/B}(\mathbf{k}'+\mathbf{G}') = H_{A/B}(\mathbf{k}'),$$
$$H_{AB}(\mathbf{k}'+\mathbf{G}') = e^{i\mathbf{G}'\cdot\mathbf{r}'_0}H_{AB}(\mathbf{k}'), \quad (A12)$$

$\mathbf{r}'_0 = \mathbf{r}'_B - \mathbf{r}'_A = (\frac{1}{2},\frac{1}{2})$. Considering the operator $\hat{g}_z$, we can find in the entire BZ

$$\left[\begin{bmatrix} 0 & m_z \\ m_z & 0 \end{bmatrix},\begin{bmatrix} H_A(\mathbf{k}') & H_{AB}(\mathbf{k}') \\ H_{BA}(\mathbf{k}') & H_B(\mathbf{k}') \end{bmatrix}\right] = 0. \quad (A13)$$

We have

$$V^\dagger\begin{bmatrix} 0 & m_z \\ m_z & 0 \end{bmatrix}V = \begin{bmatrix} -I_{5\times5} & 0 \\ 0 & I_{5\times5} \end{bmatrix}, \quad (A14)$$

$$V = \frac{1}{\sqrt{2}}\begin{bmatrix} A & A \\ B & -B \end{bmatrix}, \quad (A15)$$

with $A = I_{5\times5}, B = -m_z$. It is straightforward to check that $H_0(\mathbf{k}')$ can also be block diagonalized, i.e.,

$$V^\dagger H_0(\mathbf{k}')V = H_{11}(\mathbf{k}') \oplus H_{22}(\mathbf{k}'), \quad (A16)$$

with $H_{11}(\mathbf{k}')=H_A(\mathbf{k}') - H_{AB}(\mathbf{k}')m_z$ and $H_{22}(\mathbf{k}') = H_A(\mathbf{k}') + H_{AB}(\mathbf{k}')m_z$. From Eq. (A12), we can get $H_{A/B}(k_{x'}+2\pi n_{x'}, k_{x'}+2\pi n_{y'}) = H_{A/B}(k_{x'}+2\pi n_{x'},k_{x'}+2\pi n_{y'})$ and $H_{AB}(k_{x'}+2\pi n_{x'},k_{x'}+2\pi n_{y'}) = e^{i(2\pi n_{x'}\frac{1}{2}+2\pi n_{y'}\frac{1}{2})}H_{AB}(k_{x'}+2\pi n_{x'},k_{x'}+2\pi n_{y'})$. When $(n_{x'},n_{y'}) = (0,1)$, $H_{11}(\mathbf{k}') = H_A(\mathbf{k}') - H_{AB}(\mathbf{k}')m_z$ and $H_{22}(\mathbf{k}') = H_A(\mathbf{k}'+\mathbf{Q}') - H_{AB}(\mathbf{k}'+\mathbf{Q}')m_z$, with $\mathbf{Q}' = (0,2\pi)$. Furthermore, the momentum defined in the one-Fe BZ is $k_x = (k_{x'}+k_{y'})/2$, $k_y = (-k_{x'}+k_{y'})/2$ and $\mathbf{Q} = (\pi,\pi)$.

Under the basis, $\Psi^\dagger(\mathbf{k}) = [\psi^\dagger(\mathbf{k}),\psi^\dagger(\mathbf{k}+\mathbf{Q})]$, with $\psi^\dagger(\mathbf{k}) = [d^\dagger_{xz}(\mathbf{k}),d^\dagger_{yz}(\mathbf{k}),d^\dagger_{x^2-y^2}(\mathbf{k}),d^\dagger_{xy}(\mathbf{k}),d^\dagger_{z^2}(\mathbf{k})]$, $d_l(\mathbf{k}) = \frac{1}{\sqrt{2}}[d_{A,l}(\mathbf{k}') + d_{B,l}(\mathbf{k}')]$, and $d_l(\mathbf{k}+\mathbf{Q}) = \frac{1}{\sqrt{2}}[d_{A,l}(\mathbf{k}') - d_{B,l}(\mathbf{k}')]$ for $l = xz,yz$, $d_l(\mathbf{k}) = \frac{1}{\sqrt{2}}[d_{A,l}(\mathbf{k}') - d_{B,l}(\mathbf{k}')]$ and $d_l(\mathbf{k}+\mathbf{Q}) = \frac{1}{\sqrt{2}}[d_{A,l}(\mathbf{k}') + d_{B,l}(\mathbf{k}')]$ for $l = xy,x^2-y^2,z^2$, the TB Hamiltonian in the one-Fe BZ takes the following form:

$$H_0 = \sum_{\mathbf{k}} \Psi^\dagger(\mathbf{k})H_0(\mathbf{k})\Psi(\mathbf{k}). \quad (A17)$$

Then,

$$H_0(\mathbf{k}) = H_o(\mathbf{k}) \oplus H_e(\mathbf{k}). \quad (A18)$$

Here $H_e(\mathbf{k}) = H_o(\mathbf{k}+\mathbf{Q})$.

The TB Hamiltonian in one-Fe BZ Eq. (A18) have block-diagonal forms, and each block has definitive orbital parity with respect to the glide plane symmetry. Besides, the inversion symmetry $\hat{g}_i = \{i|\mathbf{r}_0\}$ indicates that the inversion center of monolayer FeSe is at the midpoint of the Fe-Fe link. Thus we can find that $d_{xz/yz}(\mathbf{k})/d_{xy/x^2-y^2/z^2}(\mathbf{k})$ are inversion even/odd, and $d_{xz/yz}(\mathbf{k}+\mathbf{Q})/d_{xy/x^2-y^2/z^2}(\mathbf{k}+\mathbf{Q})$ are inversion odd/even. In other words, $d_{xz/yz}$ orbitals and $d_{xy/x^2-y^2/z^2}$ orbitals have opposite parities in the subspace with definitive orbital parity. The TB Hamiltonian in the one-Fe BZ is

$$H_o(\vec{k}) = \begin{bmatrix} A_{11} & A_{12} & A_{13} & A_{14} & A_{15} \\ & A_{22} & A_{23} & A_{24} & A_{25} \\ & & A_{33} & A_{34} & A_{35} \\ & & & A_{44} & A_{45} \\ & & & & A_{55} \end{bmatrix}. \quad \text{(A19)}$$

The nonzero terms in $A(k)$ are listed as follows:

$$\begin{aligned} A_{11/22}(k) =& \epsilon_1 + 2t^{11}_{x/y}\cos k_x + 2t^{11}_{y/x}\cos k_y \\ &+ 4t^{11}_{xy}\cos k_x \cos k_y + 2t^{11}_{xx/yy}\cos 2k_x \\ &+ 2t^{11}_{yy/xx}\cos 2k_y + 4t^{11}_{xxy/yyx}\cos 2k_x \cos k_y \\ &+ 4t^{11}_{xyy/xxy}\cos k_x \cos 2k_y \\ &+ 4t^{11}_{xxyy}\cos 2k_x \cos 2k_y, \\ A_{33}(k) =& \epsilon_3 + 2t^{33}_{x}(\cos k_x + \cos k_y) + 4t^{33}_{xy}\cos k_x \cos k_y, \\ A_{44}(k) =& \epsilon_4 + 2t^{44}_{x}(\cos k_x + \cos k_y) + 4t^{44}_{xy}\cos k_x \cos k_y \\ &+ 4t^{44}_{xxy}(\cos 2k_x \cos k_y + \cos k_x \cos 2k_y) \\ &+ 4t^{44}_{xxyy}\cos 2k_x \cos 2k_y, \\ A_{55}(k) =& \epsilon_5, \\ A_{12}(k) =& -4t^{12}_{xy}\sin k_x \sin k_y, \\ A_{13/23}(k) =& \pm 2it^{13}_{x}\sin k_{y/x} \pm 4it^{13}_{xy}\sin k_{y/x}\cos k_{x/y}, \\ A_{14/24}(k) =& -2it^{14}_{x}\sin k_{x/y} + 4it^{14}_{xy}\sin k_{x/y}\cos k_{y/x}, \\ A_{15/25}(k) =& 2it^{15}_{x}\sin k_{y/x} + 4it^{15}_{xy}\sin k_{y/x}\cos k_{x/y}, \\ A_{35}(k) =& 2t^{35}_{x}(\cos k_x - \cos k_y), \\ A_{45}(k) =& -4t^{45}_{xy}\sin k_x \sin k_y. \end{aligned}$$

The on-site orbital energy is $\epsilon_1 = \epsilon_2 = 0.02, \epsilon_3 = -0.539, \epsilon_4 = 0.014, \epsilon_5 = -0.581$, and the hopping parameters for the free-standing monolayer FeSe are listed as follows [61]: $t^{11}_{x/y} = -0.08/-0.311$, $t^{11}_{xy} = 0.232$, $t^{11}_{xx/yy} = 0.009/-0.045$, $t^{11}_{xxy/yyx} = -0.016/0.019$, $t^{11}_{xxyy} = 0.02$, $t^{33}_{x} = 0.412$, $t^{33}_{xy} = -0.066$, $t^{44}_{x} = 0.063$, $t^{44}_{xy} = 0.086$, $t^{44}_{xxy} = -0.017$, $t^{44}_{xxyy} = -0.028$, $t^{12}_{xy} = 0.099$, $t^{13}_{x} = 0.3$, $t^{13}_{xy} = -0.089$, $t^{14}_{x} = 0.305$, $t^{13}_{xy} = -0.056$, $t^{15}_{x} = -0.18$, $t^{15}_{xy} = 0.146$, $t^{35}_{x} = 0.338$, $t^{45}_{xy} = -0.109$. The renormalized parameters corresponding to Fig. 1(d) in the main text are $t^{44}_{xy} = 0.066$, $t^{14}_{x} = 0.405$, $t^{11}_{x} = -0.12$. The renormalized parameters corresponding to Fig. 1(e) in the main text are $t^{44}_{xy} = 0.076$, $t^{44}_{x} = 0.183$, $t^{14}_{x} = 0.405$, $t^{11}_{x} = -0.311$, $t^{11}_{xy} = 0.19$.

TABLE III. The IRs of all the possible on-site superconducting pairing in $(\mathbf{k}, -\mathbf{k}+\mathbf{Q})$ channels.

$(\mathbf{k}, -\mathbf{k}+\mathbf{Q})$: $\Delta'(\mathbf{k})$	$c_2(z)$	$c_2(x)$	σ_d	$\{i\|\frac{1}{2}\frac{1}{2}\}'$	IR
$s_0\lambda_0$	1	1	1	-1	A_{1u}
$s_0\lambda_8$	1	1	1	-1	A_{1u}
$s_0\lambda_1$	1	-1	1	-1	B_{2u}
$s_0(\lambda_4, \lambda_6)$	$(-1,-1)$	$(1,-1)$	$s_0(\lambda_6,\lambda_4)$	(1,1)	E_g
$is_z\lambda_2$	1	1	1	-1	A_{1u}
$s_z(\lambda_5,\lambda_7)$	$(-1,-1)$	$(-1,1)$	$-s_z(\lambda_7,\lambda_5)$	(1,1)	E_g
$i(s_x,s_y)\lambda_2$	$(-1,-1)$	$(-1,1)$	$i(s_y,s_x)\lambda_2$	$(-1,-1)$	E_u
$i(s_x\lambda_5,s_y\lambda_7)$	(1,1)	(1,1)	$-i(s_y\lambda_7,s_x\lambda_5)$	(1,1)	E_g
$i(s_y\lambda_5,s_x\lambda_7)$	(1,1)	$(-1,-1)$	$-i(s_x\lambda_7,s_y\lambda_5)$	(1,1)	E_g

APPENDIX B: THE CLASSIFICATIONS FOR THE $(\mathbf{k}, -\mathbf{k}+\mathbf{Q})$ PAIRING CHANNELS FROM SYMMETRY ANALYSES

The nine GellMann matrices λ_0–λ_8 in the main text are listed as follows:

$$\lambda_0 = \begin{bmatrix} 1 & 0 & 0 \\ 0 & 1 & 0 \\ 0 & 0 & 1 \end{bmatrix}, \quad \lambda_1 = \begin{bmatrix} 0 & 1 & 0 \\ 1 & 0 & 0 \\ 0 & 0 & 0 \end{bmatrix},$$
$$\lambda_2 = \begin{bmatrix} 0 & -i & 0 \\ i & 0 & 0 \\ 0 & 0 & 0 \end{bmatrix}, \quad \lambda_3 = \begin{bmatrix} 1 & 0 & 0 \\ 0 & -1 & 0 \\ 0 & 0 & 0 \end{bmatrix},$$
$$\lambda_4 = \begin{bmatrix} 0 & 0 & 1 \\ 0 & 0 & 0 \\ 1 & 0 & 0 \end{bmatrix}, \quad \lambda_5 = \begin{bmatrix} 0 & 0 & -i \\ 0 & 0 & 0 \\ i & 0 & 0 \end{bmatrix}, \quad \text{(B1)}$$
$$\lambda_6 = \begin{bmatrix} 0 & 0 & 0 \\ 0 & 0 & 1 \\ 0 & 1 & 0 \end{bmatrix}, \quad \lambda_7 = \begin{bmatrix} 0 & 0 & 0 \\ 0 & 0 & -i \\ 0 & i & 0 \end{bmatrix},$$
$$\lambda_8 = \frac{1}{\sqrt{3}}\begin{bmatrix} 1 & 0 & 0 \\ 0 & 1 & 0 \\ 0 & 0 & -2 \end{bmatrix}.$$

TABLE IV. The IRs of all the possible non-on-site superconducting pairing in $(\mathbf{k}, -\mathbf{k}+\mathbf{Q})$ channels.

$(\mathbf{k}, -\mathbf{k}+\mathbf{Q})$: $\Delta'(\mathbf{k})$	IR
$f_{4,k}s_0\lambda_{0/8}, f_{5,k}s_0\lambda_1, f_{3,k_x}s_0\lambda_5 + f_{3,k_y}s_0\lambda_7$	A_{1u}
$f_{2,k}s_0\lambda_{0/8}, f_{3,k_x}s_0\lambda_5 - f_{3,k_y}s_0\lambda_7$	B_{1u}
$f_{2,k}s_0\lambda_1, f_{3,k_y}s_0\lambda_5 - f_{3,k_x}s_0\lambda_7$	A_{2u}
$f_{5,k}s_0\lambda_{0/8}, f_{1/4,k}s_0\lambda_1, f_{3,k_y}s_0\lambda_5 + f_{3,k_x}s_0\lambda_7$	B_{2u}
$if_{1/4,k}s_z\lambda_2, i^{1/0/0}[f_{3,k_x}s_{z/x/y}\lambda_4 + f_{3,k_y}s_{z/y/x}\lambda_6]$	A_{1u}
$if_{2,k}s_z\lambda_2, i^{1/0/0}[f_{3,k_x}s_{z/x/y}\lambda_4 - f_{3,k_y}s_{z/y/x}\lambda_6]$	B_{1u}
$i^{1/0/0}[f_{3,k_y}s_{z/x/y}\lambda_4 - f_{3,k_x}s_{z/y/x}\lambda_6]$	A_{2u}
$if_{5,k}s_z\lambda_2, i^{1/0/0}[f_{3,k_y}s_{z/x/y}\lambda_4 + f_{3,k_x}s_{z/y/x}\lambda_6]$	B_{2u}
$if_{1/2/4/5,k}(s_x,s_y)\lambda_2$	E_u

The monolayer FeSe has inversion symmetry, thus every IR in Table I should have a counterpart with an inverse parity. In other words, $(\mathbf{k},-\mathbf{k}+\mathbf{Q})$ pairing channels should be possible from the symmetry point. For the $(\mathbf{k},-\mathbf{k}+\mathbf{Q})$ pairing, we define the Nambu basis, $\Psi'(\mathbf{k}) = [\{\psi_{m\uparrow}(\mathbf{k})\},\{\psi_{m\downarrow}(\mathbf{k})\},\{\psi^\dagger_{m\downarrow}(-\mathbf{k}+\mathbf{Q})\},-\{\psi^\dagger_{m\uparrow}(-\mathbf{k}+\mathbf{Q})\}]^t$, with $\{\psi_{m\sigma}(\mathbf{k})\} = [d_{xz\sigma}(\mathbf{k}),d_{yz\sigma}(\mathbf{k}),d_{xy\sigma}(\mathbf{k})]$. The IRs for the on-site $(\mathbf{k},-\mathbf{k}+\mathbf{Q})$ pairings are summarized in Table III.

Here the matrix for $\{i|\frac{1}{2}\frac{1}{2}\}'$ is $g'_4 = s_0\eta'_4$ and $\eta'_4 = 1\oplus -1\oplus(-1)^\alpha$ with $\alpha = 1$ for d_{xz}-d_{xy} pairing and $\alpha = -1$ for d_{yz}-d_{xy} pairing. The IRs for the non-on-site $(\mathbf{k},-\mathbf{k}+\mathbf{Q})$ pairings are summarized in Table IV. We can check that all the $(\mathbf{k},-\mathbf{k}+\mathbf{Q})$ pairing channels correspond to the interband pairings, and such kinds of pairings cannot individually give an overall full gap around the Fermi surface.

[1] X.-L. Qi and S.-C. Zhang, Rev. Mod. Phys. **83**, 1057 (2011).
[2] L. Fu and C. L. Kane, Phys. Rev. Lett. **100**, 096407 (2008).
[3] J. D. Sau, R. M. Lutchyn, S. Tewari, and S. Das Sarma, Phys. Rev. Lett. **104**, 040502 (2010).
[4] L. Fu and E. Berg, Phys. Rev. Lett. **105**, 097001 (2010).
[5] Y. Kamihara, T. Watanabe, M. Hirano, and H. Hosono, J. Am. Chem. Soc. **130**, 3296 (2008).
[6] J.-X. Yin, Z. Wu, J.-H. Wang, Z.-Y. Ye, J. Gong, X.-Y. Hou, L. Shan, A. Li, X.-J. Liang, X.-X. Wu, J. Li, C.-S. Ting, Z. Wang, J.-P. Hu, P.-H. Hor, H. Ding, and S. H. Pan, Nat. Phys. **11**, 543 (2015).
[7] N. Hao and J. Hu, Phys. Rev. X **4**, 031053 (2014).
[8] X. Wu, S. Qin, Y. Liang, H. Fan, and J. Hu, arXiv:1412.3375.
[9] Q.-Y. Wang *et al.*, Chin. Phys. Lett. **29**, 037402 (2012).
[10] D. Liu *et al.*, Nat. Commun. **3**, 931 (2012).
[11] S. He *et al.*, Nat. Mater. **12**, 605 (2013).
[12] S. Tan *et al.*, Nat. Mater. **12**, 634 (2013).
[13] R. Peng *et al.*, Nat. Commun. **5**, 5044 (2014).
[14] W.-H. Zhang *et al.*, Chin. Phys. Lett. **31**, 017401 (2014).
[15] J. J. Lee *et al.*, Nature (London) **515**, 245 (2014).
[16] J.-F. Ge *et al.*, Nat. Mater. **14**, 285 (2015).
[17] Y. S. Hor, A. J. Williams, J. G. Checkelsky, P. Roushan, J. Seo, Q. Xu, H. W. Zandbergen, A. Yazdani, N. P. Ong, and R. J. Cava, Phys. Rev. Lett. **104**, 057001 (2010).
[18] S. Sasaki, M. Kriener, K. Segawa, K. Yada, Y. Tanaka, M. Sato, and Y. Ando, Phys. Rev. Lett. **107**, 217001 (2011).
[19] S. Sasaki, Z. Ren, A. A. Taskin, K. Segawa, L. Fu, and Y. Ando, Phys. Rev. Lett. **109**, 217004 (2012).
[20] Strictly speaking, the total angular momentum instead of spin is a good quantum number if spin-orbital coupling is present. However, in iron based superconductors, the orbital moment is relatively small so that the spin index is still dominant. By convention, we still use the spin instead of the total angular momentum to classify the superconducting states.
[21] J. Hu, Phys. Rev. X **3**, 031004 (2013).
[22] N. Hao and J. Hu, Phys. Rev. B **89**, 045144 (2014).
[23] A. Subedi, L. Zhang, D. J. Singh, and M. H. Du, Phys. Rev. B **78**, 134514 (2008).
[24] V. Cvetkovic and O. Vafek, Phys. Rev. B **88**, 134510 (2013).
[25] K. Liu, Z.-Y. Lu, and T. Xiang, Phys. Rev. B **85**, 235123 (2012).
[26] T. Bazhirov and M. L. Cohen, J. Phys. Condens. Matter **25**, 105506 (2013).
[27] F. Zheng, Z. Wang, W. Kang, and P. Zhang, Sci. Rep. **3**, 2213 (2013).
[28] C. Cao, P. J. Hirschfeld, and H.-P. Cheng, Phys. Rev. B **77**, 220506 (2008).
[29] D. J. Thouless, M. Kohmoto, M. P. Nightingale, and M. den Nijs, Phys. Rev. Lett. **49**, 405 (1982).
[30] D. N. Sheng, Z. Y. Weng, L. Sheng, and F. D. M. Haldane, Phys. Rev. Lett. **97**, 036808 (2006).
[31] Z. Wang, N. Hao, and P. Zhang, Phys. Rev. B **80**, 115420 (2009).
[32] C. L. Kane and E. J. Mele, Phys. Rev. Lett. **95**, 146802 (2005).
[33] N. Read and D. Green, Phys. Rev. B **61**, 10267 (2000).
[34] X.-L. Qi, T. L. Hughes, S. Raghu, and S.-C. Zhang, Phys. Rev. Lett. **102**, 187001 (2009).
[35] T. H. Hsieh and L. Fu, Phys. Rev. Lett. **108**, 107005 (2012).
[36] I. Bozovic and C. Ahn, Nat. Phys. **10**, 892 (2014).
[37] T. A. Maier, S. Graser, P. J. Hirschfeld, and D. J. Scalapino, Phys. Rev. B **83**, 100515(R) (2011).
[38] A. Kreisel, Y. Wang, T. A. Maier, P. J. Hirschfeld, and D. J. Scalapino, Phys. Rev. B **88**, 094522 (2013).
[39] Y. Zhang *et al.*, Nat. Mater. **10**, 273 (2011).
[40] M. Xu *et al.*, Phys. Rev. B **85**, 220504 (2012).
[41] C. Fang, Y.-L. Wu, R. Thomale, B. A. Bernevig, and J. Hu, Phys. Rev. X **1**, 011009 (2011).
[42] J. T. Park, G. Friemel, Y. Li, J.-H. Kim, V. Tsurkan, J. Deisenhofer, H.-A. Krug von Nidda, A. Loidl, A. Ivanov, B. Keimer, and D. S. Inosov, Phys. Rev. Lett. **107**, 177005 (2011).
[43] I. Bozovic, G. Logvenov, I. Belca, B. Narimbetov, and I. Sveklo, Phys. Rev. Lett. **89**, 107001 (2002).
[44] N. Reyren *et al.*, Science **317**, 1196 (2007).
[45] V. L. Ginzburg, Phys. Lett. **13**, 101 (1964).
[46] L. Rademaker, Y. Wang, T. Berlijn, and S. Johnston, arXiv:1507.03967.
[47] M. Yi *et al.*, arXiv:1505.06636.
[48] P. A. Lee and X.-G. Wen, Phys. Rev. B **78**, 144517 (2008).
[49] C. M. Puetter and H.-Y. Kee, Europhys. Lett. **98**, 27010 (2012).
[50] P. W. Anderson, Science **235**, 1196 (1987).
[51] K. Liu, B.-J. Zhang, and Z.-Y. Lu, Phys. Rev. B **91**, 045107 (2015).
[52] J. Hu and H. Ding, Sci. Rep. **2**, 381 (2012).
[53] Y.-M. Lu, T. Xiang, and D.-H. Lee, Nat. Phys. **10**, 634 (2014).
[54] L. C. Hebel and C. P. Slichter, Phys. Rev. **113**, 1504 (1959).
[55] Y. Nagai, Y. Ota, and M. Machida, arXiv:1504.08095.
[56] D. A. Wollman, D. J. Van Harlingen, W. C. Lee, D. M. Ginsberg, and A. J. Leggett, Phys. Rev. Lett. **71**, 2134 (1993).
[57] J. Hu and N. Hao, Phys. Rev. X **2**, 021009 (2012).
[58] K. Shiozaki and S. Fujimoto, Phys. Rev. Lett. **110**, 076804 (2013).
[59] Y. Shimizu and K. Nomura, Phys. Rev. B **91**, 195139 (2015).
[60] R. Peng *et al.*, Phys. Rev. Lett. **112**, 107001 (2014).
[61] H. Eschrig and K. Koepernik, Phys. Rev. B **80**, 104503 (2009).